

Dynamics of Angiogenesis During Wound Healing: A Coupled *In Vivo* and *In Silico* Study

MARIA J.C. MACHADO,^{*,1} MICHAEL G. WATSON,[†] ANDREA H. DEVLIN,^{*} MARK A.J. CHAPLAIN,[‡] STEVEN R. MCDUGALL,[†] AND CHRISTOPHER A. MITCHELL^{*}

^{*}Centre for Molecular Biosciences, University of Ulster, Coleraine, UK; [†]Institute of Petroleum Engineering, Heriot-Watt University, Edinburgh, UK; [‡]Division of Mathematics, University of Dundee, Dundee, UK

Address for correspondence: Dr. Christopher Mitchell, Centre for Molecular Biosciences, University of Ulster, Coleraine, BT52 1SA, UK.

E-mail: ca.mitchell@ulster.ac.uk

Dr. Steven McDougall, Institute of Petroleum Engineering, Heriot-Watt University, Edinburgh EH14 4AS, UK. E-mail: steve.mcdougall@pet.hw.ac.uk

¹Present address: INSERM U833, Collège de France, 11 place Marcelin-Berthelot, 75231 Paris Cedex 05, France.

Received 3 June 2010; accepted 30 November 2010.

ABSTRACT

Objective: The most critical determinant of restoration of tissue structure during wound healing is the re-establishment of a functional vasculature, which largely occurs via angiogenesis, specifically endothelial sprouting from the pre-existing vasculature.

Materials and Methods: We used confocal microscopy to capture sequential images of perfused vascular segments within the injured *panniculus carnosus* muscle in the mouse dorsal skin-fold window chamber to quantify a range of microcirculatory parameters during the first nine days of healing. This data was used to inform a mathematical model of sequential growth of the vascular plexus. The modeling framework mirrored the experimental circular wound domain and incorporated capillary sprouting and endothelial cell (EC) sensing of vascular endothelial growth factor gradients.

Results: Wound areas, vessel densities and vessel junction densities obtained from the corresponding virtual wound were in excellent agreement both temporally and spatially with data measured during the *in vivo* healing process. Moreover, by perturbing the proliferative ability of ECs in the mathematical

model, this leads to a severe reduction in vascular growth and poor healing. Quantitative measures from this second set of simulations were found to correlate extremely well with experimental data obtained from animals treated with an agent that targets endothelial proliferation (TNP-470).

Conclusion: Our direct combination and comparison of *in vivo* longitudinal analysis (over time in the same animal) and mathematical modeling employed in this study establishes a useful new paradigm. The virtual wound created in this study can be used to investigate a wide range of experimental hypotheses associated with wound healing, including disorders characterized by aberrant angiogenesis (e.g., diabetic models) and the effects of vascular enhancing/disrupting agents or therapeutic interventions such as hyperbaric oxygen.

Key words: angiogenesis, wound healing, dorsal skin-fold window chamber, mathematical modeling, mouse, *in vivo*

Abbreviations used: ASF, area scale factor; DSWC, dorsal skin-fold window chamber; EC, endothelial cell; FITC, fluorescein isothiocyanate; PC, panniculus carnosus; PDE, partial differential equation; VEGF, vascular endothelial growth factor; N_j , vessel junction density; ρ_v , vessel density.

Please cite this paper as: Machado, Watson, Devlin, Chaplain, McDougall and Mitchell (2011). Dynamics of Angiogenesis During Wound Healing: A Coupled *In Vivo* and *In Silico* Study. *Microcirculation* 18(3), 183–197.

INTRODUCTION

Wound healing is an essential response to injury characterized by a sequence of events involving hemostasis, inflammation, granulation tissue formation, regeneration and remodeling, which culminates in varying degrees of functional restoration of tissue structure and fibrosis [23,66]. A critical determinant of successful wound healing is the rapid re-establishment of a functional microcirculation in hypoxic tissue, which occurs via the process of

angiogenesis: the sprouting of new vessels from pre-existing vasculature [11]. As poor wound healing represents a significant burden on the healthcare system, enhancing neovascularisation continues to be a subject of intense research activity in both pre-clinical models of disease as well as in controlled clinical trials [32].

A variety of factors impact on the timing and success of regeneration following injury, including the stage of development, tissue type, size of injury, environmental factors (such as infection and temperature) and the genotype/strain

of the host [23]. In order to examine the effectors of tissue regeneration, numerous *in vivo* laboratory models of wound healing and vascular adaptation have been established, which measure specific end points from the tissue to molecular level such as wound closure, vascular density, tensile strength and matrix or chemotactic agent concentrations (reviewed in [23]). Mathematical modeling of angiogenesis has been performed at a range of scales [41], largely focussing on tumor-induced angiogenesis informed by assumptions gleaned from a variety of *in vitro* and *in vivo* experimental models [2,34,35,57,58]. Early mathematical models of wound healing have examined healing in the epidermis [54] and dermal wound contraction [40], while more recent approaches have focussed on cell migration [8,36] and oxygen based therapy in chronic wounds [15,53]. The vast majority of these models have adopted a continuum approach to angiogenesis [7,15,17,43,44,53,65] and lack the potential for quantitative comparison with living experimental vascular architectures. A number of studies have also been undertaken to examine vascular remodeling in the absence of growth [41,42]. However, these approaches do not consider endothelial migration and focus primarily upon pruning and dilation within pre-existing capillary beds. Our approach describes the first direct coupling of *in vivo* longitudinal quantitative data from an experimental wound healing study with mathematical modeling.

In order to study a highly reproducible pattern of tissue regeneration, we chose to model the revascularization of a ~1.2 mm circular lesion in the PC muscle of adult male mice [22]. We have adapted and expanded a hybrid partial differential equation (PDE)-discrete approach [34] to model angiogenesis during wound healing in the pc. The pc is an ideal model system to investigate mathematically, as it is a thin, 3–5 myofiber wide skeletal muscle layer on the dorsum of mice underlying the hypodermis, supplied by an isotropic and effectively two-dimensional regular microvascular network. Wounds induced in this muscle layer heal in a centripetal fashion [22], with a gradual reorganization of network structure, so that the microvascular architecture matches the metabolic requirements of the regenerating tissue. The model incorporates capillary sprouting from surviving vasculature induced by a vascular endothelial growth factor (VEGF) gradient [18] and endothelial cell (EC) migration determined by random motility and local sensing of chemotactic gradients. Sprout tip branching and tip–tip fusion are included. Blood is supplied to the nascent vasculature and the resulting stimuli, including wall shear stress and transmural pressure, lead to dynamic adaptation of capillary radius [34]. Full details of the relevant equations and modeling assumptions are presented in the Materials and Methods section. The *in silico* model has been validated by direct comparison with quantitative *in vivo* data. We further demonstrate the potential

of the model by reducing EC proliferation to simulate the effect of the anti-angiogenic agent TNP-470 (O-(Chloroacetylcarbonyl) fumagillol, AGM-1470), a potent synthetic analog of fumagillin [26]. TNP-470 inhibits EC proliferation by binding and inhibiting the action of the metalloprotease methionine aminopeptidase (metAP-2) [55], an enzyme responsible for amino-terminal cleavage of methionine following protein synthesis in the cell. TNP-470 dose dependently inhibits endothelial proliferation *in vitro* [30,67,68] and the measurable downstream effects of this activity *in vivo* are reductions in EC proliferation, angiogenesis and tissue growth both during tumorigenesis [26] and normal physiological processes such as adipose tissue growth [48] and in the female reproductive cycle [29,51].

The goal of this study was to establish a basic framework for a virtual wound by coupling experimental data with a parallel computational approach. This constitutes a novel approach which can subsequently be used to inform biologically testable hypotheses associated with the remodeling of vascular plexi. Overall, this study conclusively demonstrates that the robustness of a mathematical model of angiogenesis during wound healing can be effectively benchmarked against *in vivo* longitudinal data.

MATERIALS AND METHODS

In Vivo Wound Healing Model and Imaging

Prior to surgery, animals were housed under standard laboratory conditions with a 12 hour light–dark cycle. Adult 8- to 10-week-old male Balb/c mice ($n = 11$, 22–27 g) were anesthetised intraperitoneally with 10 mg/kg fluanisone, 0.3 mg/kg fentanyl citrate (Hypnorm; VetaPharma Ltd, Leeds, UK) and midazolam 5 mg/kg (Hypnovel; Roche, Welwyn, UK) before window chamber surgery was performed [22], taking care to debride the pc muscle of its overlying fascial layer on the surgically operated side. Post-operatively, mice received 20 mg/kg meloxicam analgesia sub-cutaneously (SC), (Metacam; Boehringer Ingelheim, Ingelheim, Germany), 1 ml 5% glucose solution intraperitoneally and topical chloramphenicol ointment on the suture sites (Martindale Pharmaceuticals, Romford, UK). Mice were housed in a ventilated heating cabinet at 34°C and fed with standard laboratory chow softened in water.

Three days after window chamber implantation, mice were anesthetised as previously described and then injected intravenously with 100 μ l of 50 mg/ml 150 kDa fluorescein isothiocyanate (FITC)-conjugated dextran (Sigma-Aldrich, Gillingham, UK) in saline solution into the lateral tail vein to visualize perfused vessels. The uninjured pc plexus was imaged by confocal microscopy before application of a single 100°C 10 seconds contact

wound directly to the pc, carefully placed away from large blood vessels and neurovascular bundles. The wound area was then immediately imaged by confocal microscopy with a maximum duration of approximately 20 minutes between FITC injection and post-injury imaging.

On days 3, 6, and 9 post-wounding, animals were anaesthetised and injected with FITC-conjugated dextran as previously described and immediately imaged. In order to minimize repeated administration of anesthesia, we restricted intra-vital imaging to the key time points of day 0 (pre and immediately post-wounding), day 3 (maximal macrophage infiltration), day 6 (maximal angiogenesis) and 9 days post-wounding (angiogenic remodeling). During imaging, animals were restrained in a bespoke jig and placed with the viewing side downwards on the imaging platform of a Leica SP5 confocal microscope (Leica Microsystems, Wetzlar, Germany). Revascularization of the wound occurred in the focal plane of the pc muscle (approximately 30–50 μm thick) by the radial ingrowth of angiogenic sprouts from pre-existing vessel stumps and capillaries in the zone adjacent to the area of injury as previously demonstrated [22]. Image capture was performed using a 10 \times objective with the confocal pinhole at \sim 350 μm (35 μm focal depth), so that the parallel oriented vasculature within the pc muscle was visible in a single image. Images of the wound center and the surrounding areas immediately north, south, east, and west of the wound were captured as .tif files. For the TNP-470 experiment, animals were randomly attributed to vehicle ($n = 4$) or TNP-470 treatment ($n = 4$) groups and injected sc every other day with 30 mg/kg TNP-470 [32,57] or vehicle (1% DMSO in saline) beginning on the day of wounding (day 0). All experiments were approved by the UK Home Office and conformed to the Animal (Scientific Procedures) Act 1986.

Wound Healing Histology, Immunostaining, and Ultrastructural Analysis

Adult 8- to 10-week-old male Balb/c mice (22–27 g) were anaesthetised and prepared as described previously. A full thickness incision was made on the dorsum and the skin was temporarily sutured to a custom designed frame for application of 10 seconds contact burn (100°C) wounds to the pc layer, after which the frame was removed and the skin sutured with blanket stitching. Animals were euthanized on days 3, 6, 9 and 15 post-wounding. For histology, the full thickness skin was fixed in 10% neutral buffered formalin, paraffin embedded, transverse sections were stained with hematoxylin and eosin and analysed by light microscopy using standard protocols. Whole mounted wounds were fixed for 48 hours in 4% para-formaldehyde and processed using

standard immunofluorescence protocols [18] using biotin-conjugated Isolectin B4 from *Bandeiraea simplicifolia* (*Griffonia simplicifolia*, 20 $\mu\text{g}/\text{ml}$; Sigma) and Alexa Fluor-488 streptavidin conjugate (1:100; Molecular Probes, Paisley, UK) to detect blood vessels and rat anti-mouse F4/80 (1:100; AbD Serotec, Kidlington, UK) with anti-rat rhodamine-conjugated antibody (1:100; Santa Cruz, CA, USA) to detect activated macrophages. Confocal microscopy was used to create a maximum projection image of a z-series through the pc layer of the wound. Ultrastructural analysis was performed using standard techniques. Briefly, burn wounds were fixed in Karnovsky's fixative, post-fixed in osmium tetroxide and resin embedded. Semi-thin sections were stained with 2% toluidine blue in 5% borax and examined by phase contrast microscopy, ultra thin sections were stained with uranyl acetate and lead citrate and examined on a JEOL JEM-1010 transmission electron microscope (JEOL, Tokyo, Japan) at an accelerating voltage of 80 kV.

Analysis of Wound Healing

Composite images of the wound area from the intra-vital imaging were generated in Photoshop CS4 (Adobe Systems Inc, San Jose, CA, USA) and analysed using Image J [1]. Wound area was determined as the area devoid of FITC-dextran perfused vessels. Modified "Petri-metric" stereology techniques [25] were used to determine the N_j and ρ_v . The geometric center of the wound was determined and analysis performed at 250 μm intervals directly north, south, east and west up to a distance of 750 μm . Areas which included large arterioles or venules, crossed neurovascular bundles, or vessels which were poorly focused were excluded from the analysis. As we were primarily interested in angiogenesis within the wound area and adjacent areas (which occurs from existing capillaries or post-capillary arterioles), we did not examine the vessel density in the capillary regions containing these features. At each 250 μm interval, a rectangular Merz grid (sampling area $1 \times 10^6 \mu\text{m}^2$) was centered and the number of vessel junctions (N_j) per $1 \times 10^6 \mu\text{m}^2$ was calculated using: $N_j = J/(\text{ASF})$, where J is the number of vessel junctions within the sampling frame and the ASF is calculated using the formula: $\text{ASF} = 2d^2/(10^6 \mu\text{m}^2)$, where $d(\mu\text{m})$ is the height of the sampling frame [25]. The functional vessel density (ρ_v) per $1 \times 10^6 \mu\text{m}^2$ was determined using $\rho_v = (I.d)/(\text{asf})$, where I is the number of vessels intersecting the orthogonal line of the Merz grid. The mean \pm SEM values at each interval for each time point were determined. Repeated measures one-way ANOVA (95% Confidence interval) with Bonferroni's post-test was used to test for significant differences across days within groups. Two-way repeated measures ANOVA was used to test the effect of TNP-470 treatment over time across groups. All statisti-

cal tests were performed using GraphPad Prism 3.0 (GraphPad Software, San Diego, CA, USA).

MATHEMATICAL MODELING

Modeling Vessel Network Formation via EC Migration

Since the dorsal skin-fold window chamber isolates a thin tissue region, a two-dimensional mathematical model provided an adequate representation of the ($\sim 50 \mu\text{m}$ thick) pc microvascular network. The EC migration model assumes that the tips of the new vessels have the ability to migrate through (i) random motility, (ii) chemotaxis in response to VEGF released by macrophages [4], and (iii) haptotaxis in response to gradients in the extracellular matrix (ECM). ECs produce matrix degrading enzymes, the best described of which are the matrix metalloproteases (MMPs), which diffuse and locally degrade the ECM allowing the manifestation of the haptotactic response. Denoting by n the EC density per unit area, the non-dimensional equation describing EC conservation is given by:

$$\frac{\partial n}{\partial t} = D\nabla^2 n - \nabla \cdot \left(\frac{\lambda}{1 + \delta c} n \nabla c \right) - \rho \nabla \cdot (n \nabla f). \quad (1)$$

Discretizing the above equation permits the migration of individual sprout tips on the lattice to be governed by their local environment. At each time step, the tips will either remain stationary or migrate up, down, left or right with a likelihood informed by values scaled to the relative strength of local environmental stimuli. By scaling such that these values sum to unity, the particular migration direction of each sprout tip is then determined from a set of normalized movement weights [2].

The hybrid PDE-discrete system is completed by the equations:

$$\frac{\partial c}{\partial t} = -\eta n_i c \quad (2)$$

$$\frac{\partial f}{\partial t} = \beta n_i - \gamma m f \quad (3)$$

$$\frac{\partial m}{\partial t} = \alpha n_i + \varepsilon \nabla^2 m - \nu m \quad (4)$$

where c represents the VEGF concentration, f the ECM concentration, m the MMP density and n_i a Boolean value (1 or 0) indicating the presence or absence of a tip cell at a given position. Where η , β , γ , α , ε and ν are rate constants for: VEGF uptake by EC, ECM production, ECM degradation, MMP production, MMP diffusion and MMP decay, respectively.

Modeling Blood Perfusion in the Developing Capillary Network

The wound healing process involves capillary remodeling and vessel adaptation, which can only be successfully simulated by incorporating blood flow through the evolving capillary structures [34,35]. At the scale of a single capillary element of length L and radius R , the approximate relationship between pressure gradient ΔP and flow Q takes the form of a Poiseuille-like expression:

$$Q = \frac{\pi R^4 \Delta P}{8 \mu_{\text{app}}(R, H_D) L}, \text{ with } \mu_{\text{app}}(R, H_D) = \mu_{\text{rel}} \times \mu_{\text{plasma}} \quad (5)$$

where μ_{app} is the apparent blood viscosity which depends on the local blood hematocrit (H_D), vessel radius and plasma viscosity (μ_{plasma}). By conserving mass at each node of the network, we arrive at a set of linear equations for the nodal pressures which can be solved numerically. Using these nodal pressures, we can, in turn, calculate the flow in each capillary element. As accurate experimental measurement of blood viscosity in living microvessels is difficult, we apply the relationship used in [10]:

$$\mu_{\text{rel}}(R, H_D) = \left[1 + (\mu_{0.45} - 1) f(H_D) \left(\frac{2R}{2R - 1.1} \right)^2 \right] \times \left(\frac{2R}{2R - 1.1} \right)^2 \quad (6)$$

where R is the vessel radius, and $\mu_{0.45}$ and $f(H_D)$ are the viscosity corresponding to the average human hematocrit value and a function of the hematocrit, respectively. The full parameterisation of the above relationship can be found in [58].

Vessels are capable of adapting their radii in response to various blood flow stimuli, introducing a feedback loop since the variation in radii will affect the rheological properties of the blood. The stimuli considered follow the treatment of Pries et al. [45,47], and include wall shear stress (S_{wss}), intravascular pressure (S_p) and a metabolic mechanism (S_m). The model assumes that the change in a flowing vessel radius (ΔR) over a time step Δt is proportional to both the global stimulus acting on the vessel and to the initial vessel radius R :

$$\begin{aligned} \Delta R &= S_{\text{tot}} R \Delta t = (S_{\text{wss}} + S_p + S_m) R \Delta t \\ &= \left[\log(\tau_w + \tau_{\text{ref}}) - k_p \log \tau_c(P) + \right. \\ &\quad \left. k_m \log \left(\left(\frac{Q_{\text{ref}}}{Q H_D} \right) + 1 \right) - k_s \right] R \Delta t. \end{aligned} \quad (7)$$

The constants k_p and k_m characterize the relative intensity of the pressure and metabolic stimuli, respectively, while the extra k_s term is intended to represent the natural

shrinking tendency of vessels in the absence of positive growth stimuli. Further details can be found in [34,45–47]. By coupling EC migration and perfusion—including blood rheological properties and capillary remodeling mechanisms—we can simulate, at a vascular level, the response to wounding and subsequent dynamic adaptation and remodeling of the flowing vascular network. It should be noted that while newly sprouted blind-ended vessels [22] are known to leak plasma into the wound area, erythrocytes (where occasionally present) remain largely static and the lack of perfusion in such vessels has negligible impact upon the oxygen delivery to the lesion. Predictions of network hematocrit distributions and intra-wound oxygen delivery will form the basis of a future publication.

Coupling Flow and Cell Migration through Capillary Branching and Anastomosis

The model deals with anastomosis and sprout branching in a similar manner to earlier tumor angiogenesis models [2, 34, 57, 58]. If two individual capillary sprouts meet, they will fuse to form a closed loop and may continue to grow through subsequent branching. Capillary sprout branching can only occur in tips which have reached a certain level of maturation and, additionally, the probability of branching is assumed to be correlated to the local VEGF concentration gradient. Branching induced by wall shear stress in perfused vessels (see [34]) is not considered here as our simulations predict maximum wall shear stresses in the wound area of approximately 0.5 Pa—such small stresses would not be expected to produce additional branching in perfused vessels.

Initial Model Parameterization and Simulation Details

The domain is a square of length $L = 2$ mm with an initial circular wound of radius 0.6 mm positioned at its center. There are large parent vessels at the upper and lower edges of the domain and 20 smaller parent vessels positioned evenly, between which have been ablated in the wounded area. The vascular network grows from the smaller parent vessels, with sprouts initiated at evenly spaced positions where the VEGF concentration exceeds a critical value. Zero-flux boundary conditions are imposed on all boundaries of the domain. Initially, a uniform ECM profile is assumed throughout the domain and a radially symmetric VEGF concentration profile that decreases from the wound center is set up (this effectively mimics the net result of macrophage infiltration and VEGF production during the inflammatory phase of the healing response). There are no MMPs present initially, as these are only produced once capillary sprouting has begun by tip cells [13]. The experimental data suggest a significant delay in the onset of angiogenesis after injury (two to three days) therefore,

Table 1. Parameter values used in untreated wound simulations

Parameter	Definition	Value	Source
D	EC random motility coefficient	3.0×10^{-5}	[5,49]
χ	EC chemotaxis coefficient	0.091	[5,59]
δ	EC chemotactic receptor saturation factor	0.6	[2]
ρ	EC haptotaxis coefficient	0.3	[5,61]
η	VEGF uptake by EC rate	0.1	[2]
β	ECM production rate	0.05	[2]
γ	ECM degradation rate	0.1	[2]
α	MMP production rate	1.0×10^{-6}	[3]
ε	MMP diffusion rate	0.01	[3]
ν	MMP decay rate	3.0	[3]
τ_{ref}	Reference wall shear stress	0.103 dyn/cm^2	[45]
Q_{ref}	Reference flow rate	$1.909 \times 10^{-11} \text{ m}^3/\text{s}$	[58]
k_p	Relative intensity rate of the pressure stimuli	0.1	[34]
k_m	Relative intensity rate of the metabolic stimuli	0.07	[34]
k_s	Natural shrinking rate of vessels	0.35	[34]

angiogenic sprouting commences at day 2.1 post-wounding. Unless otherwise indicated, the dimensionless cell migration and vessel remodeling parameter values used in the simulations are summarized in Table 1 (together with corresponding supporting references where available). We note that the values of D and χ have been informed by benchmarking the simulations against experimental pc data.

For all of the simulation results, the radii of the two large parent vessels and 20 smaller parent vessels were held at 12 and 4 μm , respectively, in line with experimental observations. Sprouts emerging from the parent vessels were assigned an initial radius of 3 μm before perfusion. Prior to wounding, it is assumed that all parent vessels are capable of flow and, post-wounding, the ablated vessels may regain flow due to reconnection via the angiogenic process. Each parent vessel is assumed to have a pre-formed basal lamina and does not remodel. The radii of the newly sprouted vessels were permitted to remodel from 3 μm to a maximum of 12 μm . Vascular “pruning” was achieved by removing vessel segments devoid of a critical level of hematocrit (2%) for a critical length of time (approximately 6 days), to prune vessels which received no positive growth stimulus during their lifetime.

TNP-470 Model Parameterization and Simulation Details

In order to model the effect of the TNP-470, only minor modifications to the above were considered. The main impact of the agent was assumed to be a reduction of

sprout tip chemotactic sensitivity to VEGF and reduced proliferative branching within the wound area. In order for sprout tips to advance in the migration model, it is implicitly assumed that proliferation must have occurred in the stalk cells. Therefore, by targeting the mechanisms for migration, we are inherently targeting EC proliferation. Consequently, the chemotactic parameters were modified to reflect this and a small sensitivity study showed that $\delta = 1.74$ and $\chi = 0.12$ were sufficient to reproduce the observed reduction in angiogenic response (all other parameters remained unchanged). The only other perturbation to the untreated system was a small modification to the initial conditions. This was based on the experimental observation that the TNP-470 treated mice displayed an increased wound area at day 3. Thus, in order to maintain consistency between the simulation and experiment at 2.1 days post-wounding, the initial wound radius was increased from 0.6 mm to 0.64 mm, which resulted in the ablation of some additional parent vessel segments in the vicinity of the wound edge.

***In silico* Image Analysis**

For direct comparison with *in vivo* data, vessel density (ρ_v) and vessel junction density (N_j), were sampled. Three annular regions were constructed about the wound center, with boundaries defined 80 μm either side of contours set at 250, 500, and 750 μm from the wound center, respectively. Results at the wound center were obtained from a circle of radius 80 μm . The total length of all vessel segments and the number of occurrences of branching within these four regions were calculated. Wound area was approximated by splitting the domain into four quadrants of equal area and determining the distance from the wound center to the nearest perfused vessel (i.e., a vessel having a hematocrit greater than the critical pruning value). The average of these values was then used as an approximation of the wound radius and the area of a circle characterized by this radius was calculated as an approximation to wound area.

RESULTS

The pc muscle is an approximately 3–5 myofiber wide skeletal muscle layer (30–50 mm in diameter), located between the panniculus adiposus and interstitial connective tissue layers (Figure 1A) on the dorsum of mice. Injection of 150 kDa FITC-dextran and intravital confocal microscopic imaging of a dorsal skin-fold window chamber preparation (Figure 1B) allows image capture of perfused vessels throughout the full thickness of the pc, which can be analysed by modified stereological techniques (Figure 1C: see Methods for details). At three days post-injury, numerous F4/80 reactive mononuclear cells are observed ahead of angiogenic sprouts (Figure 1D,E), evidence of the extensive

inflammatory infiltrate observed within the injury area (Figure 1F). Concomitantly, injured muscle fibers surrounding the direct injury site have sealed their ends and new myotubes have formed within this zone (Figure 1F). By day 6, collagen deposition adjacent to myofibers and myotubes is consistent with the regenerative response observed in skeletal muscle injury in the BALB/c strain. Cells with the ultrastructural features of macrophages are also observed close to immature capillaries (Figure 1G) and myotubes. Myofiber and vascular plexus regeneration are evident by day 15, as well as areas of severe disruption to muscle architecture, with numerous capillaries interspersed between large areas of cellular connective tissue (Figure 1H).

***In situ* Vascular Morphology Following Injury to the pc Muscle**

Capillaries in the uninjured murine pc muscle are arranged in a regular parallel network with prominent large diameter feeder vessels (Figure 2A). Immediately post-wounding, vessels containing FITC-dextran labeled plasma are absent from the wound area (Figure 2B) and plasma leakage is observed from dilated vessels at the wound periphery. The injury generates a non-perfused, essentially circular wound with a highly reproducible size ($1.02 \pm 0.1 \text{ mm}^2$; [day 0]; Figure 2B,I) surrounded by ~ 25 –30 pre-existing peripheral, occluded vessels. Maximal wound area occurs by day 3 ($1.25 \pm 0.1 \text{ mm}^2$; $p < 0.01$ compared with day of injury; compare Figure 2C with Figure 2B) due to the contraction of muscle fibers within the surrounding pc, when conspicuous vasodilatation of the vessels surrounding the wound is also observed.

Revascularization of the pc occurs by sprouting of surviving peri-myofibrillar vasculature surrounding the injury site beginning at day 3, peaks at day 6 and is essentially complete by day 9. The mathematical model generates vascular architectures which closely resemble the intravital imaging micrographs from days 3 to 9 (Figure 2D–H). On day 3, there is a robust angiogenic response *in vivo* consisting of a dense annular mesh of vascular sprouts at the wound perimeter (Figure 2C,D), which is reproduced by the mathematical model. By day 6, an angiogenic plexus proceeds towards the center of the wound, and a greater number of vessels in the wound area are observed both *in vivo* and in the mathematical model (Figure 2E,F). Numerous anastomoses between vessels from different sprouts are evident and perfusion within these capillary loops causes remodeling and radial adaptation to occur. As vascular remodeling has been incorporated into the mathematical model, by day 9 the vascular plexus within the wound area is shown to be composed of several dilated capillary loops together with a small number of wound-spanning vessels, which parallels the observations *in vivo* (Figure 2G,H). These larger caliber,

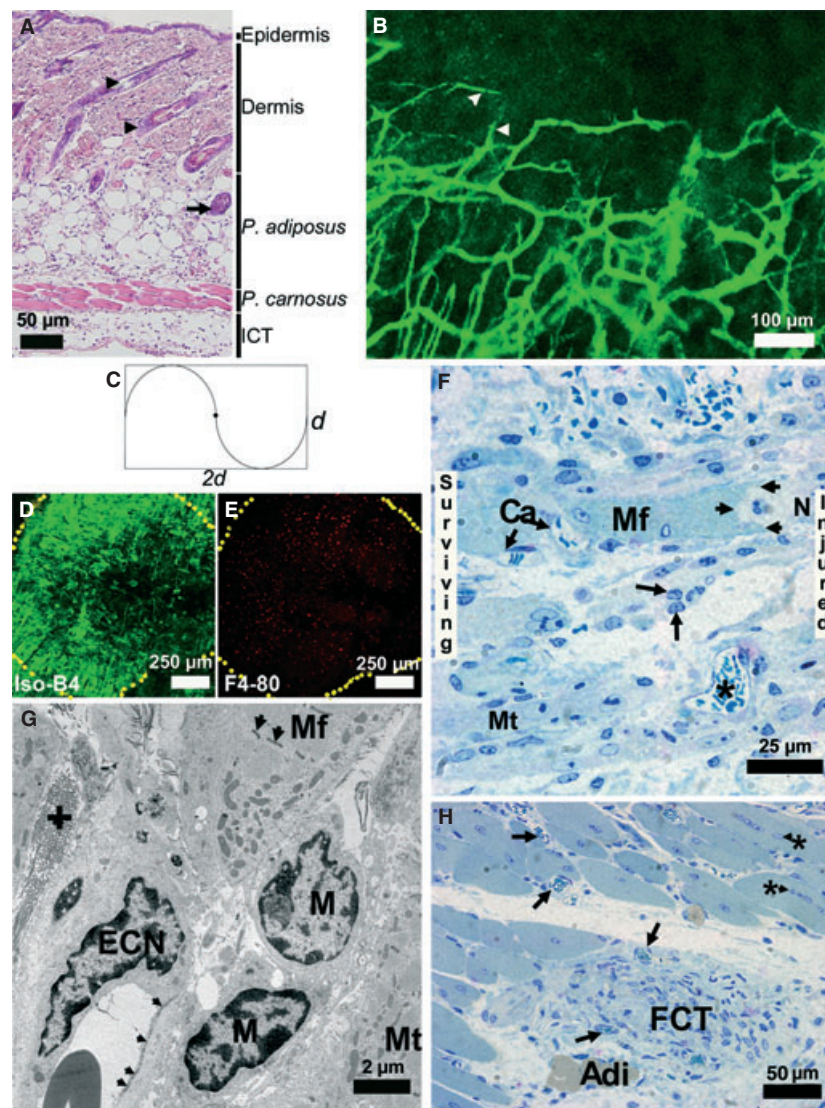


Figure 1. Morphology of the murine *panniculus carnosus* (PC) muscle. (A) Transverse, Haematoxylin & Eosin stained section of skin and underlying pc muscle from an uninjured 10-week-old male Balb/c mouse. The pc is a thin skeletal muscle layer located in subcutaneous tissue of the dorsum, between the panniculus adiposus and interstitial connective tissue (ICT). Hair follicles (arrowheads) and sweat gland (arrow) are shown in the dermal layer. (B) Representative intravital 10 \times confocal microscopic image of fluorescein isothiocyanate-dextran perfused vessels in the wounded pc, 6 days post thermal injury in the dorsal skin-fold window chamber. The wound area (top) is devoid of perfused vessels and the regenerating angiogenic plexus with blind-ended vessels (arrowheads) is conspicuous. Quantitative analysis of the pc capillary network was performed with a Merz grid (C) using modified stereological techniques (see Materials and Methods for details). (D, E) Maximum projections of Z-stack series through the pc layer of a single representative 3 days post wounded whole-mounted sample co-stained with BSI-B4 (D) and F4/80 (E). Granulation tissue and necrotic debris is non-specifically stained with BSI-B4 in addition to capillary endothelium (D) and infiltrating F4/80 reactive macrophages are distributed throughout the entire wound area (E). The wound area in both micrographs is indicated by the dotted yellow line. (F) Toluidine blue stained, semi-thin resin section of pc muscle 3 days after injury. Adjacent to the injury area, a neutrophil (N, gray arrow) is located at the sealed ends (black arrowheads) of a surviving myofiber (Mf), close to an area of hemorrhage (H). Several capillaries (Ca) are observed adjacent to the surviving Mf. A larger diameter venule (*) is seen proximal to the injury and numerous leukocytes pervade the interstitial space. A newly formed myotube (Mt) is located at the edge of the surviving tissue. (G) Electron micrograph of pc regeneration adjacent to the direct injury (bottom) area at 6 days post wounding. Several macrophages (m) with prominent lysosomes are evident in the interstitial space between a developing Mt and a mature Mf. New capillary growth is evidenced by an activated endothelial cell nucleus (containing abundant nucleopores) and continuous dense junctional complex (arrowheads). Collagen bundles (+) are also prominent. (H) Toluidine blue stained semi-thin light micrograph of regenerating pc muscle at 15 days post wounding. Numerous blood vessels (arrows) of varying in caliber are interspersed with pre-existing damaged centronucleated Mfs (arrowheads indicated by *) in the pc muscle layer. A cluster of adipocytes (Adi) is observed adjacent to an area of fibrotic connective tissue (FCT).

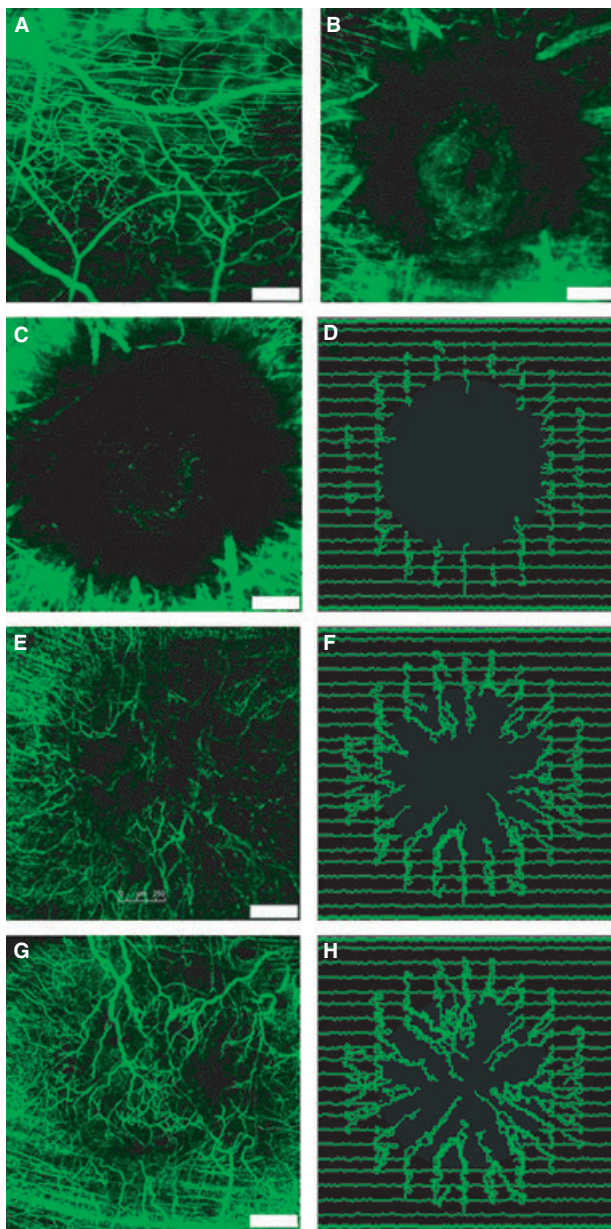


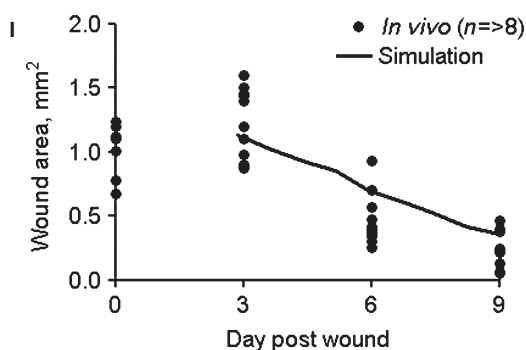
Figure 2. Qualitative comparison of *in vivo* wound healing with mathematical modeling in Balb/c mice. Confocal images of fluorescein isothiocyanate-dextran perfused vessels in the panniculus carnosus muscle within the dorsal skin-fold window-chamber of the same animal pre-wound (A) and immediately post-thermal injury (B). Features of wound healing *in vivo* (C, E, G) are recapitulated in the mathematical model (D, F, H) with vascular sprouting on day 3 (C, D), increased vessel density by day 6 (E, F) and dilated capillary loops and vessels spanning the wound area by day 9 (G, H). Scale bar = 250 μm . Wound area in each individual animal correlates with the predicted wound area in the mathematical simulation (I).

wound-spanning vessels are highly disorganized compared with uninjured tissue (cf. Figure 2G,A), although some evidence of vascular re-alignment with the long-axis of surviving myofibers is observed at the wound periphery.

Quantitative Analysis of Vascular Growth Following Injury to the pc Muscle

The mathematical model quantitatively reproduces the rate of wound closure observed *in vivo* from days 3 to 9 ($p < 0.0001$; Figure 2I). In order to standardize the collection of microcirculatory data, we sampled at the geometric center (0 μm) and at 250 μm intervals (250, 500, and 750 μm) from the center of the wound. On day 3, the wound center (0–250 μm) remains avascular (Figure 3A,B) and at the wound edge (500 μm), where the first angiogenic sprouts are detected, both the N_j and ρ_v are significantly lower than pre-injury values ($p < 0.0001$). Outside the wound boundary (on day 3, mean diameter = 610 μm), there is a significant reduction in ρ_v ($p < 0.05$) but no significant change in N_j (NS: $p > 0.05$) compared to pre-wound values. By day 6, the center of the wound contains flowing vessels, corresponding with a small increase in ρ_v ($p < 0.01$), although N_j (NS; $p > 0.05$) is unchanged. Near the edge of the wound (500 μm), significant increases in both N_j and ρ_v ($p < 0.05$) indicate a robust angiogenic response (Figure 3A,B) compared with day 3. Outside the wound boundary (750 μm), both ρ_v and N_j have already effectively returned to pre-wound values. By day 9, both N_j and ρ_v have increased significantly close to the wound center (250 μm) compared with day 6 (Figure 3A,B; $p < 0.01$), although at the center of the lesion itself (0 μm) both values still remain far lower than those observed pre-injury (compare with day 0; $p < 0.01$).

Comparison of the quantitative longitudinal data obtained *in vivo* and *in silico* provided a rigorous test of the mathematical modeling (Figure 3C–H). As *in vivo* data is inherently variable (sample size [n] = 7–11), we compared mean and median N_j and ρ_v values with data from the virtual wound. The mathematical model predictions compare very favorably both spatially and temporally



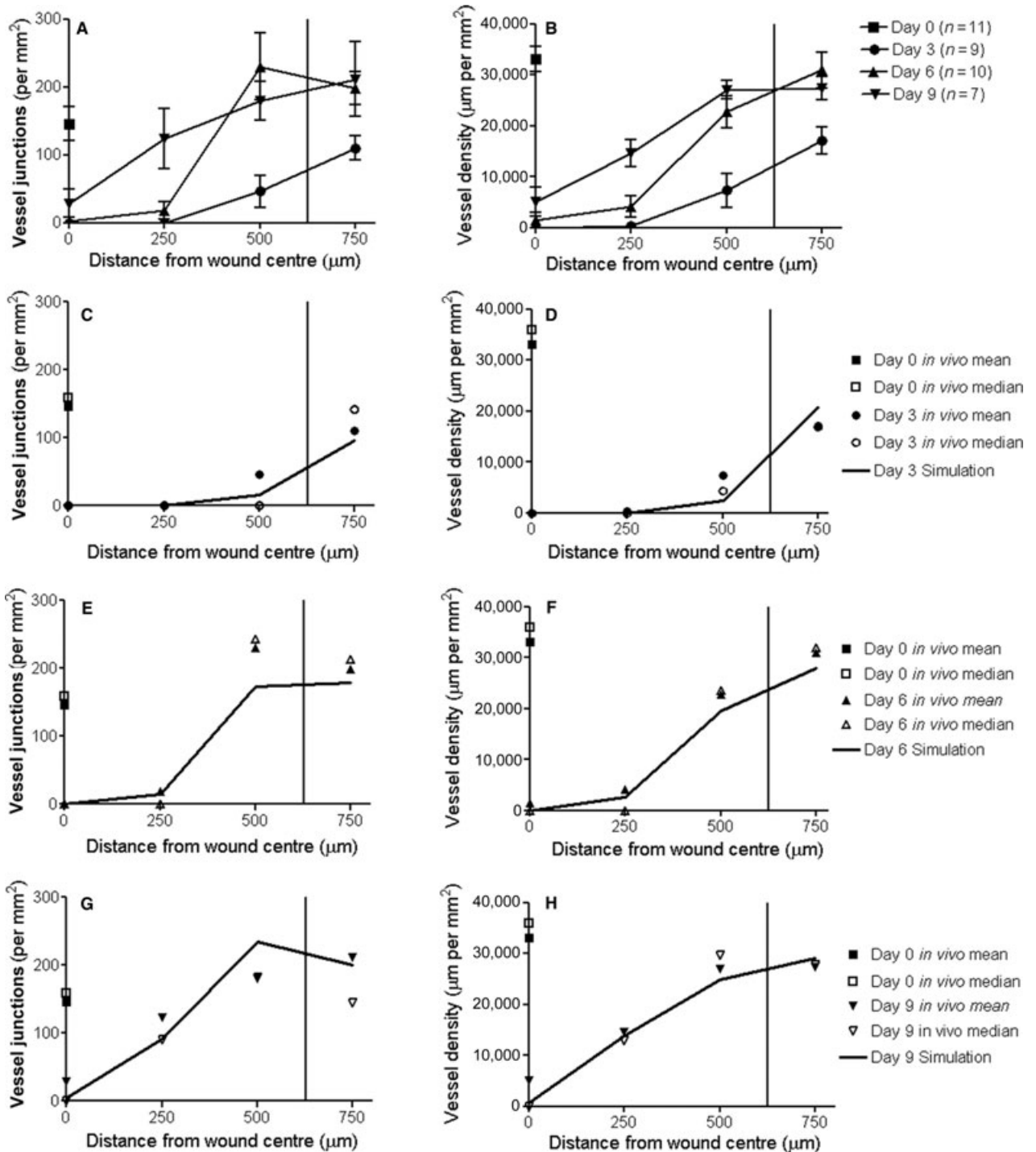


Figure 3. *In vivo* and simulated microvascular parameters in normal Balb/c mice wound healing. Vessel junction numbers (A) and functional vessel density (B) determined from fluorescein isothiocyanate-dextran perfused vessels in the panniculus carnosus preparation of the dorsal skin-fold window-chamber ($n \geq 7$, mean \pm SEM) compared with pre-injury (day 0) values. Vessel junction numbers and functional vessel density values in the mathematical model show excellent correlation with the mean and median *in vivo* values on days 3 (C, D), 6 (E, F) and 9 (G, H). The solid vertical line represents mean day 3 wound area radius.

(Figure 3) with the *in vivo* data. While the modeling slightly under-predicts N_j close to the wound edge (500 μm) at day 6 (Figure 3E) and slightly over-predicts N_j

at day 9 (Figure 3G), the ρ_v are generally in excellent agreement over the full course of the simulation (Figure 3D,F,H). Moreover, the simulations successfully

reproduce the significant increase in N_j and ρ_v observed close to the center of the lesion (250 μm) on day 9 (Figure 3G,H).

Modeling Vascular Growth Following pc Muscle Injury in TNP-470 Treated Animals

The effect on vascular growth and wound area was investigated in mice treated with the anti-angiogenic agent TNP-470. As TNP-470 reduces EC proliferation, the only modifications to the base model described above were (i) reduced chemotactic sensitivity of sprout tips to VEGF, and (ii) reduced likelihood of EC branching. The intracellular mechanism of action of TNP-470 has been characterized through *in vitro* studies and mediated by the inhibition of metAP2, an enzyme responsible for methionine cleavage from pre-proteins. However, in the current model, we are primarily concerned with the net effect of TNP-470 at the cellular level; namely that the speed of capillary migration and proclivity for branching are compromised. All other parameters remained unchanged and there was no attempt to optimize the model in order to fit experimental data.

In situ Morphology Following Injury of pc Muscle in TNP-470 Treated Animals

Immediately post-wounding, the wound area is similar in both vehicle and TNP-470 treated animals (Figure 4A; $p > 0.05$). Wound area decreases in both groups between days 0 and 9 ($p < 0.0001$). However, in the TNP-470 treated group, there is a significant delay in wound closure compared to the vehicle group, particularly between days 3–6 (Figure 4A; $p < 0.05$). In animals treated with TNP-470, the wound area is larger on day 3 (Figure 4A) compared with vehicle treated animals ($p < 0.05$). In order to remain consistent with the experimental system, the initial wound radius was increased from 0.6 to 0.64 mm. The TNP-470 mathematical model successfully predicted reduced wound healing in TNP-470 treated animals, closely matching the *in vivo* data (Figure 4A).

The qualitative impact of TNP-470 treatment within the healing wound and the simulation is presented in Figure 4B–G. Fewer vessel sprouts are observed around the wound periphery on day 3 compared with untreated animals (Figure 4B cf. Figure 2C) and this is recapitulated in the mathematical model (Figure 4C cf. Figure 2D). The increased wound area observed at day 6 in TNP-470 treated animals is consistent with a reduced angiogenic response *in vivo* (Figure 4D cf. Figure 2E) and in the simulation (Figure 4E cf. Figure 2F). Similarly, by day 9, the extent of capillary migration both *in vivo* and in the model is greatly suppressed leading to a severe reduction in the number of perfused vessels and a complete absence of anastomosed vessels spanning the lesion (Figure 4F,G), which are numerous in the untreated animals and model (Figure 2G,H).

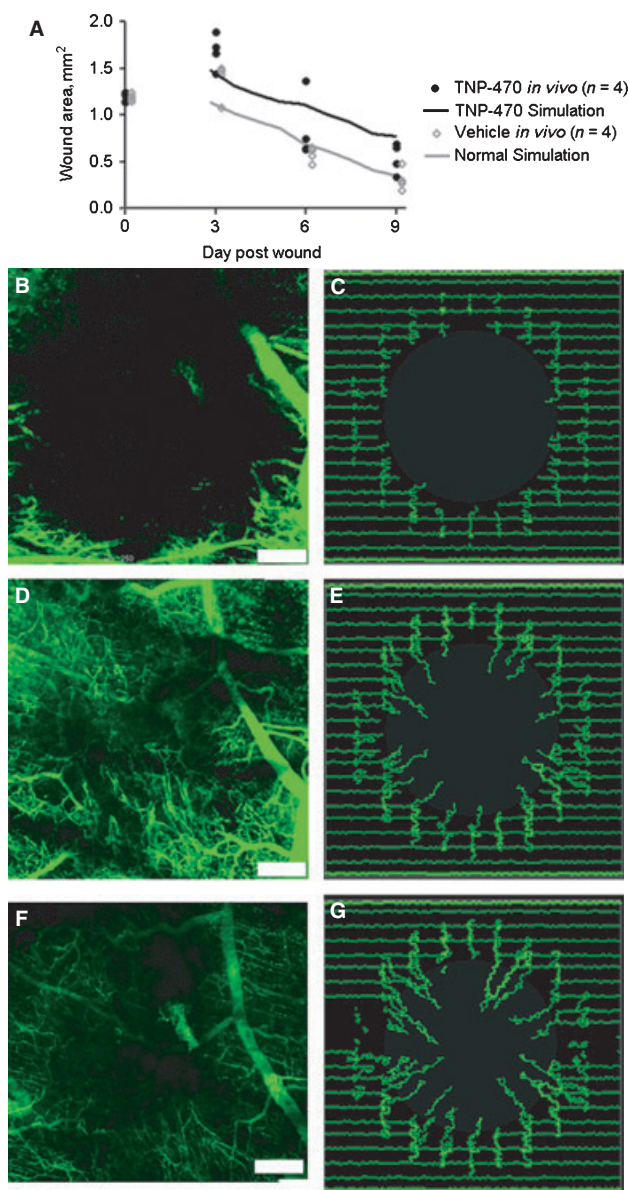


Figure 4. Qualitative comparison of *in vivo* wound healing with mathematical modeling in TNP-470 treated animals. Wound area in the murine panniculus carnosus preparation of the dorsal skin-fold window chamber in Balb/c mice treated with the anti-angiogenic agent TNP-470 ($n = 4$) and vehicle treated mice ($n = 4$) compares well with the mathematical model (A). Composite confocal images of fluorescein isothiocyanate-dextran perfused vessels of the same animal treated with TNP-470 indicate that the mathematical model accurately predicts the effect of anti-angiogenic agents *in vivo*. TNP-470 treatment leads to a larger wound area on day 3, with a reduced number of sprouts (B, C compared with untreated animals, Figure 2). By day 6, reduced sprouting observed *in vivo* (D) is mirrored in the simulation (E). At day 9, TNP-470 delayed wound healing is characterized by a reduction in the number of anastomosed vessels and delayed migration of endothelial cells in both the *in vivo* (F) and simulated images (G). Scale bar = 250 μm .

Quantitative Analysis of Vascular Growth Following Injury of the pc Muscle in TNP-470 Treated Animals

The effect of TNP-470 on microcirculatory parameters *in vivo* is presented in Figure 5. On day 3, there is no significant effect of TNP-470 treatment, though ρ_v and N_j are significantly lower than day 0 pre-injury values in both groups ($p < 0.0001$; Figure 5A,B). By day 6, an angiogenic response is evident near the edge (500 μm) of the wound in the vehicle treated animals, with a significant increase in N_j compared with day 3 ($p < 0.05$). However, N_j is significantly lower in animals treated with TNP-470. ($p < 0.01$; Figure 5C) compared with vehicle treated animals. TNP-470 treated animals also exhibited a lower ρ_v on day 6 compared with vehicle treated animals, although these differences were not statistically significant (Figure 5D). By day 9, the angiogenic plexus has invaded further into the wound in the vehicle treated animals, with both N_j and ρ_v approaching pre-injury values (Figure 5E,F). In TNP-470 treated animals, both N_j and ρ_v are significantly decreased ($p < 0.05$) compared with controls (Figure 5E,F), with no significant change in either N_j and ρ_v between days 6 and 9.

A comparison of *in vivo* quantitative data with data from the mathematical model is shown in Figure 6. The mathematical model predicts the observed delay in advancement of the angiogenic plexus towards the wound center, characterized at days 6 and 9 by decreased N_j (Figure 6B,C) and ρ_v (Figure 6E,F) when compared with the mean and median values of TNP-470 treated animals, confirming the robustness of the mathematical model.

DISCUSSION

The pc dorsal skin-fold window chamber (DSWC) wound-healing protocol described in this study is particularly suitable for mathematical modeling, as arteriolar, venular, capillary [31,60] or blind-ended microvascular segments [22] from the same regions of interest can be imaged in the same animal over time, generating longitudinal data sets for analysis. Focal heat-injury to the pc produces a standardized, circular, non-perfused wound area with a reproducible size and shape, allowing quantification of angiogenesis and regeneration in both a spatially and temporally defined manner, which is critical for mathematical modeling [9,20,22].

The *in vivo* data was used to inform a robust mathematical model, employing a hybrid discrete-PDE formulation. During normal wound healing, the *in silico* model qualitatively and quantitatively reproduces the sequential changes of the vasculature *in vivo*. Functional capillary density (ρ_v), an important microcirculatory parameter which is easily measurable in skeletal muscle tissue, is very sensitive to changes in metabolic status, such as those experienced during exercise-induced hypertrophy [56]. Functional capillary density in the center of virtual and pc wounds increases over days 3–9 post-wounding, consistent with the centripetal progression in the leading edge of the advancing vascular network [22] and previously observed in classical wound healing studies [12,52]. Comparison of ρ_v and N_j at 3, 6, and 9 days post-injury in the virtual wound show excellent correlation with *in vivo* observations in the DSWC and also qualitatively reproduce vascular architectures and capillary

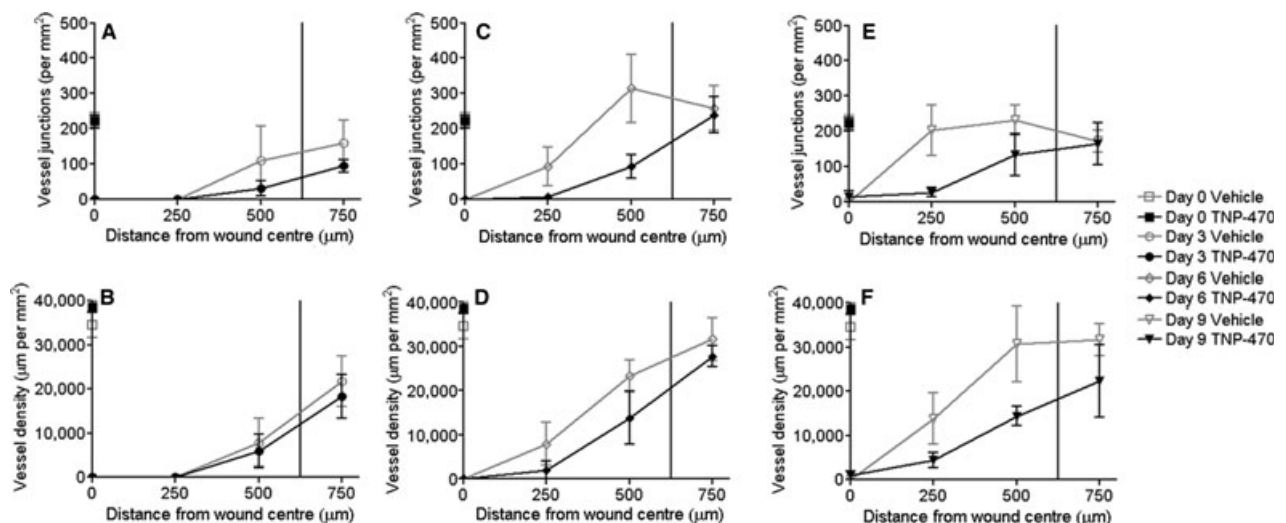


Figure 5. Quantitative analysis of *in vivo* wound healing in TNP-470 treated Balb/c mice. Vessel junction number on days (A) 3, (C) 6, and (E) 9 post-wounding, functional vessel density on days (B) 3, (D) 6, and (F) 9 post-wounding determined from fluorescein isothiocyanate-dextran perfused vessels in the panniculus carnosus preparation of the dorsal skin-fold window-chamber of TNP-470 or vehicle treated mice ($n = 4$, mean \pm SEM) compared with pre-injury (day 0) values. Mean avascular wound radius on day 3 is indicated by the solid vertical line.

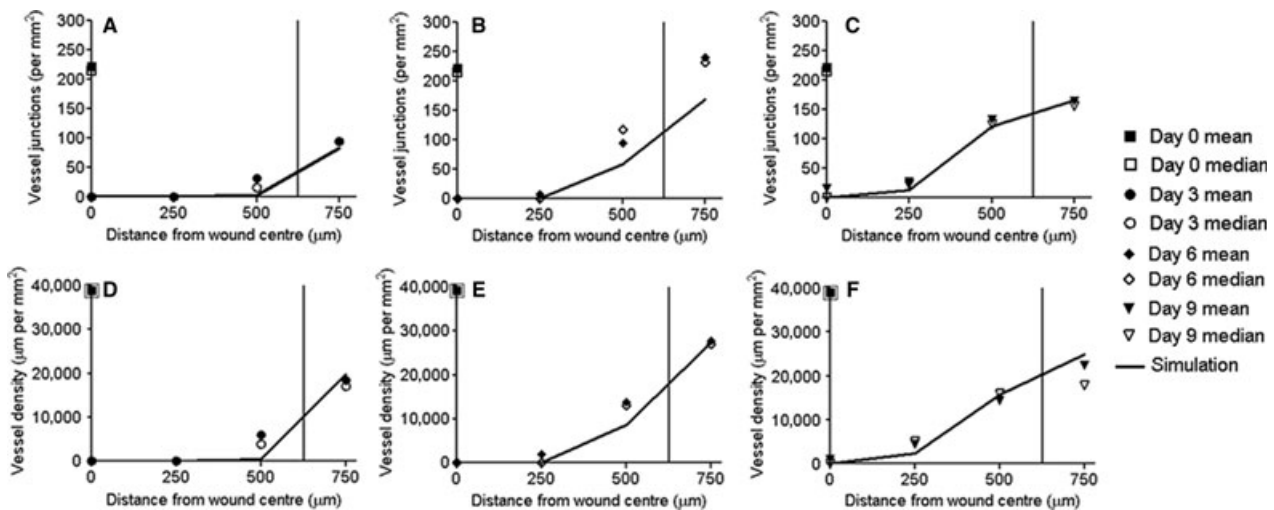


Figure 6. Comparison of *in vivo* and simulated microvascular parameters during wound healing in TNP-470 treated Balb/c mice. Microcirculatory parameters determined from perfused vessels in the murine pc in the dorsal skin-fold window-chamber mice treated with the anti-angiogenic agent TNP-470 and the corresponding mathematical simulation. There is a good agreement between the mean and median vessel junction number (A–C) and vessel density (D–F) values determined *in vivo* on days 3 to 9 with the mathematical model (solid line). The solid vertical line represents mean day 3 wound area radius.

morphologies. Although evidence of vascular re-structuring was clearly observed *in vivo* on day 9, wound closure was not complete, consistent with a previous finding of impaired skeletal muscle regeneration in Balb/c mice [38]. We and other groups have previously described strain-specific regenerative responses following skeletal muscle injury. For instance, regeneration of functional muscle tissue and parallel organization of the microvasculature in BALB/c mice is severely affected by a persistence of necrotic debris [38] and fibrotic tissue formation, which is similar to the regenerative pattern in large traumatic muscle injuries in humans [21]. The regenerative capacity of injured skeletal muscle [28,37,38] is associated with strain-specific characteristics of the host, which are at least partially mediated by pre-existing arteriolar architecture [33], the efficiency of phagocytosis of necrotic myofibrillar debris and the extent of fibrosis [38].

To date, mathematical modeling of vasculature has been largely restricted to angiogenesis and tumor growth [2,34,35,41,57,58] or flow related phenomena in individual vascular segments [22,45]. These models are validated by qualitative comparisons with biological data accumulated from a variety of different models and groups. In contrast, this is the first study to directly compare morphological data from a mathematical model with data obtained during longitudinal experiments of wound healing, other than studies predicting crude wound closure rates *in vivo* [9,10]. The present model does not include the individual contribution of all cell types involved in wound healing. For instance, invading inflammatory cells are not explicitly incorporated, but the release of pro-angiogenic factors to

promote wound healing from these cells is simulated by the VEGF gradient in the model and the role of infiltrating fibroblasts and their effect upon vascular architecture is modeled at the net level of the ECM. The model presented in this manuscript is the first stage towards the development of a complete *in silico* virtual wound, where the inclusion of inflammatory cells, fibroblasts and additional cell types involved in wound healing will form the basis for future studies.

We further tested the robustness of the mathematical model by investigating its ability to reproduce the effect of systemic administration of an anti-angiogenic agent, TNP-470, into the wound environment. TNP-470 blocks S-phase entry of EC's, actively preventing their proliferation [55]. This was effectively modeled mathematically by decreasing the likelihood of branching and reducing chemotactic sensitivity, effectively slowing down EC migration. The *in silico* model reproduced the *in vivo* effects of TNP-470, with delayed vessel growth into the wound core resulting in fewer anastomosed vessels and a large region devoid of vasculature at day 9.

Wound healing and tumor growth are both regulated by angiogenesis [11,23], a process controlled by cell migration [63], tissue oxygenation [14], cellular injury [24], red blood cell velocity, blood flow and wall shear rate [62], vascular permeability [19] and adhesion of platelets [64] or leukocytes [16] to the luminal side of the vascular wall in perfused microvessels. An exciting prospect of this modeling approach is that future iterations of the model can be further informed and refined by incorporation of quantitative data on dynamic aspects of microvascular development

measurable in the DSWC injury model [6,27]. Data from a wide variety of wild-type and transgenic mice strains, such as the non-obese diabetic mouse model of diabetes [39] whose capacities for tissue regeneration recapitulate the spectrum of responses in human wound healing, could also be incorporated in future iterations to yield important insights into the genetic, molecular and cellular responses to wound healing in healthy and diseased tissues.

The mathematical model presented in this study accurately simulates the sequential angiogenic responses observed in healing wounds and the effects of therapeutic intervention, and will be used to formulate novel hypotheses that are testable *in vivo*. We are extending and adapting this interdisciplinary approach to model vascular development in other organ systems, such as the retina

(unpublished data) and tumor progression. The novel combined *in vivo* and mathematical modeling approach described in this study provides evidence for the benefits of a new experimental paradigm in which longitudinal *in vivo* data can be used to directly inform modeling and rigorously test the accuracy of *in silico* predictions.

ACKNOWLEDGMENTS

The authors gratefully acknowledge the support of the BBSRC grant BB/F002254/1. We also wish to thank Prof. Moritz A. Könerding and Mrs. Kerstin Bähr for assistance with electron microscopy.

REFERENCES

- Abramoff MD, Magelhaes PJ, Ram SJ. Image processing with ImageJ. *Biophotonics Int* 11: 36–42, 2004.
- Anderson AR, Chaplain MAJ. Continuous and discrete mathematical models of tumor-induced angiogenesis. *Bull Math Biol* 60: 857–899, 1998.
- Anderson ARA, Chaplain MAJ, Newman EL, Steele RJC, Thompson AM. Mathematical modelling of tumour invasion and metastasis. *J Theor Med* 2: 129–154, 2000.
- Barrientos S, Stojadinovic O, Golinko MS, Brem H, Tomic-Canic M. Growth factors and cytokines in wound healing. *Wound Repair Regen* 16: 585–601, 2008.
- Bray D. Cell Movements. New York: Garland Publishing, 1992.
- Brown EB, Campbell RB, Tsuzuki Y, Xu L, Carmeliet P, Fukumura D, Jain RK. In vivo measurement of gene expression, angiogenesis and physiological function in tumors using multiphoton laser scanning microscopy. *Nat Med* 7: 864–868, 2001.
- Byrne HM, Chaplain MAJ, Evans DL, Hopkinson J. Mathematical modelling of angiogenesis in wound healing. *J Theor Med* 2: 175–197, 2000.
- Cai AQ, Landman KA, Hughes BD. Multi-scale modeling of a wound-healing cell migration assay. *J Theor Biol* 245: 576–594, 2007.
- Cardinal M, Eisenbud DE, Phillips T, Harding K. Early healing rates and wound area measurements are reliable predictors of later complete wound closure. *Wound Repair Regen* 16: 19–22, 2008.
- Cardinal M, Phillips T, Eisenbud DE, Harding K, Mansbridge J, Armstrong DG. Non-linear modeling of venous leg ulcer healing rates. *BMC Dermatol* 9: 2, 2009.
- Carmeliet P, Jain RK. Angiogenesis in cancer and other diseases. *Nature* 407: 249–257, 2000.
- Cliff WJ, Levene CI, Sanders AG. The effect of lathyrogenic compounds on collagen formation in the rabbit ear-chamber. *J Pathol Bacteriol* 85: 257–262, 1963.
- Del Toro R, Prahst C, Mathivet T, Siegfried G, Kaminker JS, Larrivee B, Breant C, Duarte A, Takakura N, Fukamizu A, Penninger J, Eichmann A. Identification and functional analysis of endothelial tip cell-enriched genes. *Blood* 116: 4025–4033, 2010.
- Dewhirst MW, Gustafson C, Gross JF, Tso CY. Temporal effects of 5.0 Gy radiation in healing subcutaneous microvasculature of a dorsal flap window chamber. *Radiat Res* 112: 581–591, 1987.
- Flegg JA, McElwain DL, Byrne HM, Turner IW. A three species model to simulate application of hyperbaric oxygen therapy to chronic wounds. *PLoS Comput Biol* 5: e1000451, 2009.
- Gaber MW, Yuan H, Killmar JT, Naimark MD, Kiani MF, Merchant TE. An intravital microscopy study of radiation-induced changes in permeability and leukocyte-endothelial cell interactions in the microvessels of the rat pia mater and cremaster muscle. *Brain Res Brain Res Protoc* 13: 1–10, 2004.
- Gaffney EA, Pugh K, Maini PK, Arnold F. Investigating a simple model of cutaneous wound healing angiogenesis. *J Math Biol* 45: 337–374, 2002.
- Gerhardt H, Golding M, Fruttiger M, Ruhrberg C, Lundkvist A, Abramsson A, Jeltsch M, Mitchell C, Alitalo K, Shima D, Betsholtz C. VEGF guides angiogenic sprouting utilizing endothelial tip cell filopodia. *J Cell Biol* 161: 1163–1177, 2003.
- Gerlowski LE, Jain RK. Microvascular permeability of normal and neoplastic tissues. *Microvasc Res* 31: 288–305, 1986.
- Goertz O, Vogelpohl J, Jettkant B, Daigler A, Steinau HU, Steintraesser L, Langer S. Burn model for in vivo investigations of microcirculatory changes. *Eplasty* 9: e13, 2009.
- Grounds MD. Age-associated changes in the response of skeletal muscle cells to exercise and regeneration. *Ann N Y Acad Sci* 854: 78–91, 1998.
- Guerreiro-Lucas LA, Pop SR, Machado MJ, Ma YL, Waters SL, Richardson G, Saetzler K, Jensen OE, Mitchell CA. Experimental and theoretical modelling of blind-ended vessels within a developing angiogenic plexus. *Microvasc Res* 76: 161–168, 2008.
- Gurtner GC, Werner S, Barrandon Y, Longaker MT. Wound repair and regeneration. *Nature* 453: 314–321, 2008.
- Harris AG, Steinbauer M, Leiderer R, Messmer K. Role of leukocyte plugging and edema in skeletal muscle ischemia-reperfusion injury. *Am J Physiol* 273: H989–H996, 1997.
- Howard CV, Reed MG. Unbiased Stereology. New York: BIOS Scientific Publishers, 2005.
- Ingber D, Fujita T, Kishimoto S, Sudo K, Kanamaru T, Brem H, Folkman J. Synthetic analogues of fumagillin that inhibit angiogenesis and suppress tumour growth. *Nature* 348: 555–557, 1990.
- Jain RK, Munn LL, Fukumura D. Dissecting tumour pathophysiology using intravital microscopy. *Nat Rev Cancer* 2: 266–276, 2002.
- Kay PH, Mitchell CA, Akkari A, Papadimitriou JM. Association of an unusual form of a Pax7-like gene with increased

- efficiency of skeletal muscle regeneration. *Gene* 163: 171–177, 1995.
29. Klauber N, Rohan RM, Flynn E, D'Amato RJ. Critical components of the female reproductive pathway are suppressed by the angiogenesis inhibitor AGM-1470. *Nat Med* 3: 443–446, 1997.
 30. Kumeda SI, Deguchi A, Toi M, Omura S, Umezawa K. Induction of G1 arrest and selective growth inhibition by lactacystin in human umbilical vein endothelial cells. *Anticancer Res* 19: 3961–3968, 1999.
 31. Lehr HA, Leunig M, Menger MD, Nolte D, Messmer K. Dorsal skinfold chamber technique for intravital microscopy in nude mice. *Am J Pathol* 143: 1055–1062, 1993.
 32. Loges S, Roncal C, Carmeliet P. Development of targeted angiogenic medicine. *J Thromb Haemost* 7: 21–33, 2009.
 33. Mac Gabhann F, Peirce SM. Collateral capillary arterIALIZATION following arteriolar ligation in murine skeletal muscle. *Microcirculation* 17: 333–347, 2010.
 34. McDougall SR, Anderson AR, Chaplain MAJ. Mathematical modelling of dynamic adaptive tumour-induced angiogenesis: clinical implications and therapeutic targeting strategies. *J Theor Biol* 241: 564–589, 2006.
 35. McDougall SR, Anderson AR, Chaplain MAJ, Sherratt JA. Mathematical modelling of flow through vascular networks: implications for tumour-induced angiogenesis and chemotherapy strategies. *Bull Math Biol* 64: 673–702, 2002.
 36. McDougall SR, Dallon J, Sherratt JA, Maini PK. Fibroblast migration and collagen deposition during dermal wound healing: mathematical modelling and clinical implications. *Philos Trans R Soc Lond A* 364: 1385–1405, 2006.
 37. Mitchell CA, Grounds MD, Papadimitriou JM. The genotype of bone-marrow-derived inflammatory cells does not account for differences in skeletal-muscle regeneration between SJL/J and Balb/C mice. *Cell Tissue Res* 280: 407–413, 1995.
 38. Mitchell CA, McGeachie JK, Grounds MD. Cellular differences in the regeneration of murine skeletal muscle: a quantitative histological study in SJL/J and BALB/c mice. *Cell Tissue Res* 269: 159–166, 1992.
 39. Nishimoto H, Kikutani H, Yamamura K, Kishimoto T. Prevention of autoimmune insulinitis by expression of I-E molecules in NOD mice. *Nature* 328: 432–434, 1987.
 40. Olsen L, Sherratt JA, Maini PK. A mechanochemical model for adult dermal wound contraction and the permanence of the contracted tissue displacement profile. *J Theor Biol* 177: 113–128, 1995.
 41. Peirce SM. Computational and mathematical modeling of angiogenesis. *Microcirculation* 15: 739–751, 2008.
 42. Peirce SM, Price RJ, Skalak TC. Spatial and temporal control of angiogenesis and arterIALIZATION using focal applications of VEGF164 and Ang-1. *Am J Physiol Heart Circ Physiol* 286: H918–H925, 2004.
 43. Pettet GJ, Byrne HM, McElwain DL, Norbury J. A model of wound-healing angiogenesis in soft tissue. *Math Biosci* 136: 35–63, 1996.
 44. Pettet GJ, Chaplain MAJ, Evans DL, Hopkinson J. On the role of angiogenesis in wound healing. *Proc R Soc Lond B Biol Sci* 263: 1487–1493, 2000.
 45. Pries AR, Reglin B, Secomb TW. Structural adaptation of microvascular networks: functional roles of adaptive responses. *Am J Physiol Heart Circ Physiol* 281: H1015–H1025, 2001.
 46. Pries AR, Reglin B, Secomb TW. Structural adaptation of vascular networks: role of the pressure response. *Hypertension* 38: 1476–1479, 2001.
 47. Pries AR, Secomb TW, Gaegtgens P. Structural adaptation and stability of microvascular networks: theory and simulations. *Am J Physiol* 275: H349–H360, 1998.
 48. Rupnick MA, Panigrahy D, Zhang CY, Dalabrida SM, Lowell BB, Langer R, Folkman MJ. Adipose tissue mass can be regulated through the vasculature. *Proc Natl Acad Sci U S A* 99: 10730–10735, 2002.
 49. Rupnick MA, Stokes CL, Williams SK, Lauffenburger DA. Quantitative analysis of random motility of human microvessel endothelial cells using a linear under-agarose assay. *Lab Invest* 59: 363–372, 1988.
 50. Rutland CS, Jiang K, Soff GA, Mitchell CA. Maternal administration of anti-angiogenic agents, TNP-470 and Angiostatin 4.5, induces fetal microphthalmia. *Mol Vis* 15: 1260–1269, 2009.
 51. Rutland CS, Mukhopadhyay M, Underwood S, Clyde N, Mayhew TM, Mitchell CA. Induction of intrauterine growth restriction by reducing placental vascular growth with the angioinhibin TNP-470. *Biol Reprod* 73: 1164–1173, 2005.
 52. Schoefl GI. Studies on inflammation. iii. Growing capillaries: their structure and permeability. *Virchows Arch Pathol Anat Physiol Klin Med* 337: 97–141, 1963.
 53. Schugart RC, Friedman A, Zhao R, Sen CK. Wound angiogenesis as a function of tissue oxygen tension: a mathematical model. *Proc Natl Acad Sci U S A* 105: 2628–2633, 2008.
 54. Sherratt JA, Murray JD. Models of epidermal wound healing. *Proc Biol Sci* 241: 29–36, 1990.
 55. Sin N, Meng L, Wang MQ, Wen JJ, Bornmann WG, Crews CM. The anti-angiogenic agent fumagillin covalently binds and inhibits the methionine aminopeptidase, MetAP-2. *Proc Natl Acad Sci U S A* 94: 6099–6103, 1997.
 56. Soares JM. Effects of training on muscle capillary pattern: intermittent vs continuous exercise. *J Sports Med Phys Fitness* 32: 123–127, 1992.
 57. Stephanou A, McDougall SR, Anderson ARA, Chaplain MAJ. Mathematical modelling of flow in 2D and 3D vascular networks: applications to anti-angiogenic and chemotherapeutic drug strategies. *Math Comput Modell* 41: 1137–1156, 2005.
 58. Stephanou A, McDougall SR, Anderson ARA, Chaplain MAJ. Mathematical modelling of the influence of blood rheological properties upon adaptive tumour-induced angiogenesis. *Math Comput Modell* 44: 96–123, 2006.
 59. Stokes CL, Rupnick MA, Williams SK, Lauffenburger DA. Chemotaxis of human microvessel endothelial cells in response to acidic fibroblast growth factor. *Lab Invest* 63: 657–668, 1990.
 60. Tauber S, Menger MD, Lehr HA. Microvascular in vivo assessment of reperfusion injury: significance of prostaglandin E(1) and I(2) in postischemic “no-reflow” and “reflow-paradox”. *J Surg Res* 120: 1–11, 2004.
 61. Terranova VP, DiFlorio R, Lyall RM, Hic S, Friesel R, Maciag T. Human endothelial cells are chemotactic to endothelial cell growth factor and heparin. *J Cell Biol* 101: 2330–2334, 1985.
 62. Tozer GM, Prise VE, Wilson J, Cemazar M, Shan S, Dewhurst MW, Barber PR, Vojnovic B, Chaplin DJ. Mechanisms associated with tumor vascular shut-down induced by combretastatin A-4 phosphate: intravital microscopy and measurement of vascular permeability. *Cancer Res* 61: 6413–6422, 2001.
 63. Vajkoczy P, Goldbrunner R, Farhadi M, Vince G, Schilling L, Tonn JC, Schmiedek P, Menger MD. Glioma cell migration is associated with glioma-induced angiogenesis in vivo. *Int J Dev Neurosci* 17: 557–563, 1999.
 64. Vollmar B, Slotta JE, Nickels RM, Wenzel E, Menger MD. Comparative analysis of platelet isolation techniques for the in vivo study of the microcirculation. *Microcirculation* 10: 143–152, 2003.
 65. Xue C, Friedman A, Sen CK. A mathematical model of ischemic cutaneous wounds. *Proc Natl Acad Sci U S A* 106: 16782–16787, 2009.
 66. Yang GP, Lim IJ, Phan TT, Lorenz HP, Longaker MT. From scarless fetal wounds

- to keloids: molecular studies in wound healing. *Wound Repair Regen* 11: 411–418, 2003.
67. Yeh JR, Mohan R, Crews CM. The antiangiogenic agent TNP-470 requires p53 and p21CIP/WAF for endothelial cell growth arrest. *Proc Natl Acad Sci U S A* 97: 12782–12787, 2000.
68. Zhang Y, Griffith EC, Sage J, Jacks T, Liu JO. Cell cycle inhibition by the antiangiogenic agent TNP-470 is mediated by p53 and p21WAF1/CIP1. *Proc Natl Acad Sci U S A* 97: 6427–6432, 2000.